P and *S* tomography using normal-mode and surface waves data with a neighbourhood algorithm

Caroline Beghein, Joseph S. Resovsky and Jeannot Trampert

Department of Earth Sciences, Utrecht University, Budapestlaan 4, PO Box 80021, 3508 *TA Utrecht, The Netherlands. E-mail: beghein@geo.uu.nl*

SUMMARY

Traditionally *P*- and *S*-wave tomography has been based on the inversion of data that are sensitive to the desired Earth structure, and model covariance is estimated from imperfect resolution and data error propagation. This analysis ignores the usually large null-spaces, and hence the significant non-uniqueness of the solution encountered in seismic tomography problems. Here we perform a model space search for *P*- and *S*-velocity structure to find acceptable fits to recent normal-mode splitting and fundamental-mode phase velocity data. The survey of the model space employs the neighbourhood algorithm of Sambridge, which preferentially samples the good data-fitting regions. A Bayesian approach is used subsequently to extract robust information from the ensemble of models. We particularly focus on posterior marginal probability density functions and covariances for the various model parameters. The covariance matrix obtained is very useful in providing insights into the trade-offs between the different variables and the uncertainties associated with them. We stay within the framework of perturbation theory, meaning that our emphasis is on the null-space of the linear inverse problem rather than the neglected non-linearity. The whole model space (including the null-space) is sampled within reasonable parameter bounds, and hence the error bars are determined by all fitting models rather than subjective prior information. We estimated *P* and *S* models for spherical harmonic degree two only. The uncertainties are quite large and corresponding relative errors can exceed 100 per cent in the mid-mantle for V_p. We find a good correlation of our most likely *S* model with previous models but some small changes in amplitude. Our most likely *P* model differs quite strongly from the recent *P* model SB10L18 and the correlation between our most likely *P* and *S* models is small. Among all the good data-fitting models, there are, however, many that have a significant $V_p - V_s$ correlation. We compute $d \ln V_s / d \ln V_p$ from the models that correlate significantly. We find an increase with depth in the top 1500 km. Deeper in the mantle, normal-mode data prefer modest values compared with traveltime data.

Key words: error bars, neighbourhood algorithm, normal modes, seismic lower mantle tomography, surface waves.

1 INTRODUCTION

Several tomographic models of the Earth's mantle have been produced over the past 15 years, using different kinds of data, parametrizations and inversion techniques. Although there are some robust patterns, the models present large discrepancies (Resovsky & Ritzwoller 1999a). This is partly the result of the propagation of data errors through the inversion operator and imperfect resolution. Tomographic inverse problems are generally ill-posed (owing to uneven and inadequate sampling of the Earth and inadequate model parametrization) and ill-conditioned (small errors in the data can lead to large variations in the model estimation owing to very small eigenvalues) resulting in large data and model null-spaces. These null-spaces are usually dealt with by employing some kind of regularization (i.e. choosing one particular model out of many that

are compatible with the data). Different authors use different regularization schemes and hence produce discrepancies in the models obtained. We propose to sample the model space to gain an overview of all models compatible with the data rather than choosing one by some subjective regularization.

An example of how a model null-space component can change the resulting model is shown by Deal *et al.* (1999). They have been able to incorporate additional, independent information in a tomographic image without affecting the misfit. They have added a thermal model of a subducting plate to a high-resolution, 3-D tomographic study of the Tonga–Fiji region. Since the thermal model did not fit the seismic data, they added only the component of the theoretical slab that was insensitive to the seismic data using their null-space shuttle. As the vectors of the null-space have no effect on the data prediction, the new tomographic model is in equally good agreement with the data.

Unless the employed regularization is derived from true physical information, it can add artefacts to the tomographic model.

A second advantage of mapping the model space is in error analysis. Most linearized inversions give a posterior model covariance that is smaller than or equal to the prior covariance by construction (Tarantola 1987). If the cost function to be minimized has a large valley (i.e. there is a large model null-space), the posterior covariance can be seriously underestimated, depending on the prior covariance (Trampert 1998). We argue that the width of the valley in the cost function is a realistic representation of the error bars in the absence of true physical prior information.

Here we propose to use a forward modelling approach in order to explore the model space, including the null-space. We suppose that perturbation theory is valid for our forward modelling. This means that the estimated error bars take the null-space of the linear inverse problem into account, but cannot account for the neglected non-linearity in the forward problem. Since we do not make an inversion, our results are not biased by the introduction of damping or any other unphysical *a priori* information and since we stay within the linear theory, the starting model is irrelevant. We apply the neighbourhood algorithm (NA) of Sambridge (1999a) to survey the parameter space and to find an ensemble of mostly 'good' data-fitting models. This method is a novel direct search technique, conceptually very simple and able to exhibit a self-adaptive behaviour by sampling preferentially the regions of lower misfit. Once the survey of the parameter space is achieved, robust information on the ensemble can be extracted using a Bayesian approach, giving valuable indications of the errors and the correlation of the model parameters (Sambridge 1999b). We applied this method to recent normal-mode splitting measurements and fundamental surface wave velocity maps. The normal modes provide constraints on the long-wavelength structure of the Earth, for compressional and shear wave anomalies in the mantle. Fundamental-mode Rayleigh waves have been included to constrain the upper mantle. The main purpose of this work is to establish the feasibility of our approach to mantle tomography. Consequently, we concentrate only on degree-two structure.

An ensemble of 'good' data-fitting joint shear and compressional wave velocity models are produced with the present set of normal-mode and phase velocity data, and probabilistic information is retrieved. Error bars are then assigned to tomographic models. Having obtained the most likely $d \ln V_s$, $d \ln V_p$ models and their respective error bars we examine their correlation and their ratio, a quantity widely discussed in the mineral physics community and which is of particular interest for geodynamists.

2 DATA AND PARAMETRIZATION

The data set we use is composed of normal-mode splitting functions and fundamental-mode phase velocity models, corrected for the crustal model of Mooney *et al.* (1998). The free oscillations of a spherically symmetric, non-rotating and (transversely) isotropic Earth model have specific degenerate frequencies. The addition of asphericities and a slight general anisotropy (under the conditions of application of perturbation theory) generate the splitting of multiplets into singlets with eigenfrequencies close to the degenerate eigenfrequency. Let us represent these 3-D model perturbations $\delta\mathbf{m}$ (r, θ, ϕ) from the reference model in terms of spherical harmonic components:

$$\delta\mathbf{m}(r, \theta, \phi) = \sum_{s=0}^{s_{max}} \sum_{t=-s}^{s} \delta\mathbf{m}_s^t(r) Y_s^t(\theta, \phi), \tag{1}$$

where Y_s^t are fully normalized and orthogonal spherical harmonics as defined in Edmonds (1960), with harmonic degree s and azimuthal order t. The structure coefficients $_kc_s^t$ of a particular isolated multiplet (denoted by k) characterize the way in which the eigenfrequencies split. If we neglect boundary perturbations, except for the crustal correction, we are left to first order with a single linearized relation between Earth structure and structure coefficients:

$$_kc_s^t = \int_0^a \delta\mathbf{m}_s^t(r)_k\mathbf{M}_s(r)r^2\, dr, \tag{2}$$

where a is the radius of the Earth and $_k\mathbf{M}_s(r)$ is the volumetric structure kernel for the perturbation $\delta\mathbf{m}_s^t$ (with respect to PREM; see Dziewonski & Anderson 1981). For more details concerning normal-mode theory we refer the reader to Woodhouse & Dahlen (1978) or Dahlen & Tromp (1998). Normal-mode splitting measurements below 3 mHz have been made recently by Resovsky & Ritzwoller (1998) for coupled and uncoupled multiplets with good sensitivity to *S*- and *P*-velocity anomalies everywhere in the mantle.

In addition to structure coefficients, they also estimated corresponding error bars using Monte Carlo simulations of the effect of theoretical errors and noise. The structure coefficient measurements are used to create synthetic seismograms that are first perturbed with 'errors' and noise of the appropriate statistical characteristics and then inverted for new coefficient estimates. The results of multiple calculations were observed to produce approximately Gaussian coefficient distributions, the widths of which provided the uncertainties. The coefficients of different angular and azimuthal orders were also observed to vary independently. Both measurements and estimated error bars can be found on the internet (http://phys-geophys.colorado.edu/geophysics/nm.dir/). We use their degree-two structure coefficients, determined from uncoupled normal-mode multiplets, but we exclude modes with sensitivity to the inner core. We keep measurements for 82 uncoupled mode multiplets; in particular, 51 spheroidal modes and 31 toroidal modes.

To constrain the uppermost mantle, we add eight fundamental-mode Rayleigh wave phase velocity models between periods of 40 and 275 s. For periods of between 40 and 150 s, the models and errors are the average and standard deviation obtained from different studies: (Trampert & Woodhouse 1995, 1996, 2001; Ekström *et al.* 1997; Laske & Masters 1996; Wong 1989; van Heijst & Woodhouse 1999). For larger periods, we use the models of Wong (1989). 3-D models of phase velocity perturbations $\delta c/c$ (δc is the phase velocity perturbation relative to a reference phase velocity c, PREM in this case) can be expanded into spherical harmonics and their coefficients $\delta c_s^t/c$ are related to the Earth's 3-D structure in a way similar to structure coefficients:

$$_l\left(\frac{\delta c_s^t}{c}\right) = \int_0^a \delta\mathbf{m}_s^t(r)_l\mathbf{K}(r)r^2\, dr. \tag{3}$$

Note that kernels for phase velocity perturbations are independent of degree s (they all correspond to kernels with $s = 0$), unlike the kernels relative to structure coefficients, and neither of them depends on t. l is an index that discriminates between different frequencies.

Unlike for normal-mode splitting data, error bars on phase velocity maps are harder to obtain. Trampert & Woodhouse (2001) have shown that the quality of published phase velocity models vary widely with the period. At each selected period, we took all existing models, averaged each spherical harmonic coefficient and estimated its standard deviation. This should account for different measuring techniques of phase velocity, different data coverage and different regularization schemes in the construction of the maps. The error bars determined for normal-mode structure coefficients
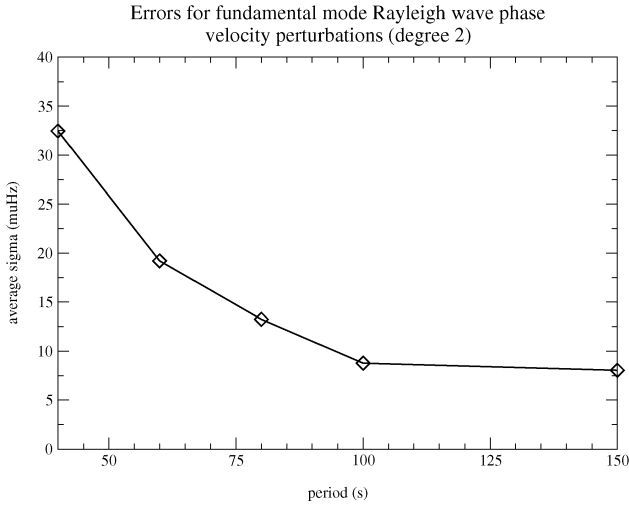
Errors for fundamental mode Rayleigh wave phase
velocity perturbations (degree 2)

Figure 1. Estimated errors for degree-two fundamental-mode Rayleigh wave phase velocity perturbations.

by Resovsky & Ritzwoller (1998) have the characteristic of being almost constant at a given degree. There is not much variation between the different orders of the spherical harmonic coefficient. By analogy, we decide to assign average uncertainties to $_l(\delta c_s^t/c)$ independent of the order t of spherical harmonic and defined by

$$\sigma_l^2 = \frac{1}{2s+1} \sum_{t=1}^{2s+1} {}_l\sigma_s^{t\,2},$$ (4)

where s is the degree of the spherical harmonic (two in this study) and $_l\sigma_s^{t\,2}$ is the variance estimated for one particular spherical harmonic coefficient. Fig. 1 shows σ_l as a function of the period of the surface waves considered. It appears that the error decreases almost linearly between 40 and 100 s and the curve flattens between 100 and 150 s. We thus decided to assign a constant uncertainty to models with periods of between 150 and 275 s, the value computed at 150 s (the model of Wong (1989) being the only one available to us at longer periods). We suppose for convenience that the errors are Gaussian distributed, but there are far too few models to test this hypothesis.

In order to implement the first part of the neighbourhood algorithm (sampling the parameter space), we need to define the fit of a model to the data. Given a data set $\mathbf{d}$, the posterior probability density (PPD) for a model $\mathbf{m}$ is given by

$$P(\mathbf{m} \,|\, \mathbf{d}) = k\beta(\mathbf{m})L(\mathbf{d} \,|\, \mathbf{m}),$$ (5)

where $\beta(\mathbf{m})$ is a prior density probability distribution and $L(\mathbf{m} \,|\, \mathbf{d})$ is a likelihood function, related to the fit of the model to the data. We take

$$\ln(P(\mathbf{m} \,|\, \mathbf{d})) = -\frac{N}{2}\chi^2$$ (6)

with

$$\chi^2 = \frac{1}{N} \left\{ \sum_{k=1}^{N_m} \frac{\left({}_k c_s^{t,\mathrm{th}} - {}_k c_s^{t,\mathrm{obs}}\right)^2}{\sigma_k^2} \right.$$

$$\left. + \sum_{l=1}^{N_s} \frac{\left[{}_l\left(\delta c_s^t/c\right)^{\mathrm{th}} - {}_l\left(\delta c_s^t/c\right)^{\mathrm{obs}}\right]^2}{\sigma_l^2} \right\}$$ (7)

where N is the total number of data points, N_m is the number of normal-mode data points and N_s is the number of surface wave

data points. The superscript 'th' denotes the theoretical structure coefficients and phase velocity perturbations, predicted by eqs (2) and (3), and 'obs' refers to the measurements. σ_k (σ_l) is the estimated error bar corresponding to the kth (lth) data. χ is a measure of the average data misfit compared with the size of the error bar.

We parametrize our models with independent isotropic perturbations of the elastic coefficients δA and δL (with $A = \kappa + \frac{4}{3}\mu = \rho V_p^2$ and $L = \mu = \rho V_s^2$) with respect to PREM. Where PREM is transversely anisotropic (at depths between 24 and 220 km), we use the equivalent isotropic PREM. The notation A and L was introduced by Love (1927) and is usually used to describe radially anisotropic media. The corresponding sensitivity kernels are given in Tanimoto (1986), Mochizuki (1986) or Dahlen & Tromp (1998). We derived the appropriate isotropic kernels and finally $\delta\mathbf{m}$ corresponds to $(\delta A, \delta L, \delta\rho)$. With the present set of normal-mode data it is not possible to resolve 3-D density perturbations in the mantle. Several authors have confirmed this (Resovsky & Ritzwoller 1999b; Resovsky & Trampert 2001; Romanowicz 2001). Instead, we decided to scale density anomalies $\delta\rho$ and shear wave velocity perturbations using $d \ln V_s/d \ln \rho = 2.5$ (Anderson *et al.* 1968). Beside the size of the model space, this constraint is the only prior information we introduce in the problem. Our models are parametrized radially in seven layers. The bottom and top depths of these layers are, in kilometres (2891, 2609), (2609, 2018), (2018, 1526), (1526, 1001), (1001, 670), (670, 220), (220, 24). They correspond to radial knots of PREM and are based on the layers defined in Resovsky & Ritzwoller (1998), which in turn are based on a Backus–Gilbert style resolution analysis (Backus & Gilbert 1968). We gathered some of their layers into one new layer in order to reduce the number of variables. Eq. (2) reduces consequently to a sum over these seven layers:

$$_k c_s^t = \sum_{i=1}^{7} \delta\overline{\mathbf{m}}_s^{t,i} \, {}_k\overline{\mathbf{M}}_s^i$$ (8)

with

$$_k\overline{\mathbf{M}}_s^i = \int_{r_i^{\mathrm{inf}}}^{r_i^{\mathrm{sup}}} {}_k\mathbf{M}_s(r) r^2 \, dr$$ (9)

where r_i^{inf} and r_i^{sup} are the lower and upper radii, respectively, of layer i and $\delta\overline{\mathbf{m}}_s^{t,i}$ is an average perturbation of parameter $\mathbf{m}_s^t$ on layer i. A similar relation holds for fundamental-mode phase velocity perturbations (eq. 3). The lateral parametrization is given in spherical harmonics by

$$\delta A(r, \theta, \phi) = \sum_{s=0}^{s_{\max}} \sum_{t=-s}^{s} \delta A_s^t(r) Y_s^t(\theta, \phi)$$ (10)

$$\delta L(r, \theta, \phi) = \sum_{s=0}^{s_{\max}} \sum_{t=-s}^{s} \delta L_s^t(r) Y_s^t(\theta, \phi).$$ (11)

These expansions allow us to solve the problem spherical harmonic coefficient by spherical harmonic coefficient. Because of the scaling relationship between $d \ln V_s$ and $d \ln \rho$, we are left with just two parameters in each layer, and thus 14 model components for each structure coefficient, or phase velocity coefficient.

3 RESULTS

3.1 Sampling and appraisal

We apply the NA using a linearized forward problem (eqs 2 and 3). We want to survey the model space to find combinations of parameters $\delta A_s^t(r)$ and $\delta L_s^t(r)$ that give an acceptable fit to the data

(eq. 7). Because there is assumed to be no covariance among the data of different angular or azimuthal order, each of the five spherical harmonic coefficients at degree two can be treated independently. In other words, we can explore five parameter spaces separately, with 14 unknowns in each of them.

First, we had to fix the boundaries of the model space. We computed the equivalent degree-two parameters $\delta L_s^t(r)$ for six different S models (MM2-L12D8, Resovsky & Ritzwoller 1999a; SKS12-WM13, Su *et al.* 1994; S20RTS, Ritsema & Van Heijst 2000; SAW12D, Li & Romanovwicz 1996; S16B30, Masters *et al.* 1996 and SB10L18, Masters *et al.* 2000). In each layer, we chose to search twice the range of the largest absolute amplitude obtained from those six models. Because model SB10L18 is a joint P and S model, we have a P model we can use to fix the range of the parameter $\delta A_s^t(r)$. We compared the amplitude of the coefficient $\delta A_s^t(r)$ corresponding to model SB10L18 and those obtained by scaling (by a factor of 2) the other S models. We fix our range for the parameter δA_s^t as twice the absolute amplitude of the largest δA_s^t found. The final result depends on the range chosen (even if the model space is completely sampled, because there is a possibility that a good fitting model exists outside this range), but because of fear of violating perturbation theory, we decided not to increase the range any further. At the same time, we ensure that these six S models are included in the model space we sample, as well as their corresponding P models. Fixing the boundaries is equivalent to equating $\beta(\mathbf{m})$ in eq. (5) to a boxcar function. This will introduce boundary effects and $P(\mathbf{m} \mid \mathbf{d})$ will not necessarily be Gaussian when the most likely model is close to the edge.

We refer the reader to Sambridge (1999a) for details concerning the sampling neighbourhood algorithm. The first stage of the algorithm, the sampling, makes use of a geometrical construct, the Voronoi cells, to approximate the misfit function and to drive the search towards the best data-fitting regions while continuing to sample a relatively wide variety of different models. It is relatively easy to tune since only two parameters have to be set: n_s, the number of models generated at each iteration, and n_r the number of 'best' data-fitting Voronoi cells in which random walks are performed at each iteration. We have been careful with the choice of these values since it is very important to have a good initial sampling in order to make a meaningful Bayesian interpretation (which is the second stage of the neighbourhood algorithm). We have to avoid directing the search towards a local minimum and we must try to sample the posterior probability density (PPD) with the highest possible accuracy, to sample all the good fitting regions of the model space. A way to do so is by increasing the values of the tuning parameters. As both tuning parameters increase together, the algorithm is more explorative as a sampler but also less efficient at mapping details of the most important (the best-fitting) parts of the model space. It is not possible to draw general conclusions on the tuning parameters since every problem is different and requires specific parameters. We had to find their most appropriate values by trial and error. Sambridge (1998) explains that the minimum sample size required is very sensitive to the dimension of the problem. His experiments show that, to obtain a good enough approximation of the posterior probability density, the required sample sizes have to be increased when the dimension of the problem becomes larger. We decided to have n_s equal to n_r, which is the minimum value n_s can take, in order to broaden the survey. We started to sample the model space with some relatively low values of n_s and n_r (10 or 20), and we increased the tuning parameters successively and compared the different results. For some variables, we obtain different results if we use such small values. This indicates that for these tuning parameters, the results

are not independent of tuning. The chosen values of n_r are not large enough to identify all the models compatible with the data. After some trials with n_r ranging up to 200, we decided to use $n_r = 50$. It is the smallest value above which the results appear to be independent of the tuning and that explores all the good-fitting regions. The algorithm is very effective in finding the regions of lowest misfit. To choose the number of iterations, we looked at the evolution of the misfit with time. χ decreases very rapidly, the sampling being directed towards the cells having the best fit. We decided to stop the survey when the misfit has 'flattened', and the model distribution is observed to approximate a likelihood sampling. The latter condition indicates that the sampling is adequate for analysis using the NA Bayesian resampling (see below). When n_r is increased, more models must be generated and hence the survey requires more time. The sampling is completed in about 2 h on a SUN Ultrasparc machine (400 MHz) for $n_r = 200$ and 300 iterations and it only takes half an hour for $n_r = 50$ and 600 iterations.

As an example, in Fig. 2 we show the result using the real part of c_2^1 in four of our seven layers. It is a way to depict the shape of the model space with regions of higher misfit (in blue) and regions of better fit (redish), where the sampling density is larger. We see that there is a clear global minimum in the upper mantle. For some other variables, the best-fitting region is more elongated. This shows that, within the boundaries of our model space, a large range of values for these variables are compatible with the data. It is the case of perturbations in $\delta A = \delta(\rho V_p^2)$ in the mid-mantle and deeper in the mantle. Several variables have their global minimum situated at the edges of the model space. Increasing the range of the survey has the effect of reducing the minimum misfit somewhat but, because of the trade-offs among the model parameters (visible in the correlation matrix, Fig. 3), moving the global minimum of one of them implies that other variables move as well and may, in turn, be directed towards the edge. Therefore, we believe that, as long as there are trade-offs between model parameters, the model space cannot be surveyed, completely guaranteeing that no solution is on the edge of the model space. This is not a major problem though, because we can quantify the trade-offs as explained below. Furthermore, increasing the range of the search substantially will violate perturbation theory and require a complete new set-up of the problem.

We now need to extract quantitative information on the models previously generated. Sambridge (1999b) provides an approach to the appraisal problem, based on a Bayesian point of view. This is the second stage of the algorithm. This appraisal of the ensemble is the most time-consuming part of the algorithm. In most model space search techniques, inferences are drawn from the good-fitting part of the ensemble only, and sometimes even from a single member. What is new in this algorithm is that the entire ensemble is used, the 'bad' data-fitting models as well as the 'good' ones, and an efficient summary of the sampled models is provided. In a Bayesian approach, the information contained in the models is represented by a posterior probability density function—in the absence of restrictive prior information on the models, the model that maximizes the PPD is the model with the best data fit. The PPD can be used to compute quantities such as the posterior mean model, the posterior model covariance matrix and marginal posterior probability density functions. An integration over the parameter space is performed using a 'likelihood sampling', the density of which corresponds to the PPD. To do this, the algorithm uses the misfit of the sampling to create a likelihood sampling. This requires a new ensemble of points to be generated (the 'resampled' ensemble), the distribution of which follows the approximate PPD. This is one of the main factors influencing the computation time. Once the resampling is done,

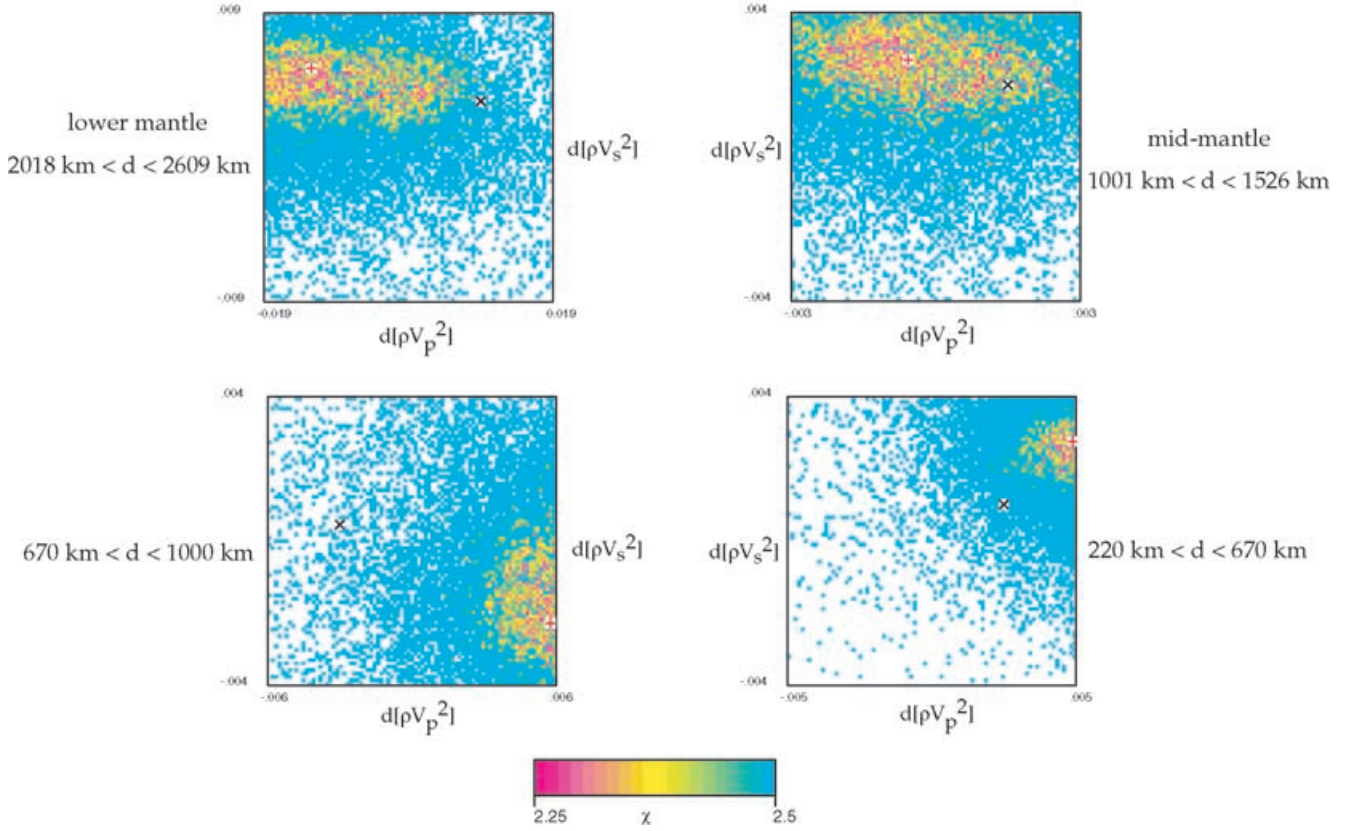## Models generated by neighbourhood algorithm

Figure 2. Results of the sampling using the real part of c_2^1 ($\delta c_2^1/c$). The colour scale represents the χ misfit as defined in eq. (7). Parameters on the horizontal axis correspond to perturbations in elastic coefficient A ($= \delta(\rho V_p^2)$) and parameters on the vertical axis correspond to perturbations in L ($= \delta\mu = \delta(\rho V_s^2)$), with respect to PREM. The full range of the models space is shown.

computing the Bayesian integrals requires only simple averages over the resampled ensemble. For more details concerning this method, see Sambridge (1999b).

For the resampling of the model space, tuning parameters have to be set: the number of random walks to perform and the number of steps per random walk. Finding the parameters that optimize the coverage of the Gibbs sampler is a trial and error process, which is time consuming but it is a characteristic of every direct search technique. It is preferable to use multiple random walks instead of a single one, and the number of steps per walk must be large enough to ensure convergence. After each trial, convergence can be checked, numerical errors evaluated and the length and number of random walks can then be adjusted accordingly. For ensembles generated with 50 cells and 600 iterations, we needed between 6000 and 10 000 steps per walk, depending on the coefficient treated, and four to six walks in order to achieve the convergence of the integrals. It takes approximately 7 h on a SUN Ultrasparc (400 MHz) to compute 1-D marginals, 2-D marginals and the correlation matrix. We also computed Bayesian integrals for some of the ensembles generated with 200 cells, to make sure that the results were the same as those obtained with 50 cells. Since their sampling required more iterations, more points are needed for the computation of the integrals. The appraisal then requires 3–4 days.

When the PPD is Gaussian, the trade-off between model parameters can be represented by the correlation matrix, which is derived from the off-diagonals of the posterior model covariance matrix. The correlation matrix corresponding to our problem is different for each spherical harmonic coefficient. The one obtained for the real part of c_2^1 is represented in Fig. 3. We can see that variables of the mid-mantle and lower mantle are highly correlated with one another. They are also correlated with model parameters of the upper mantle, for instance δA between 2018 and 2609 km of depth (layer 2) with δL in the uppermost layer. There are, to some extent, trade-offs among all the model parameters. In order to improve these
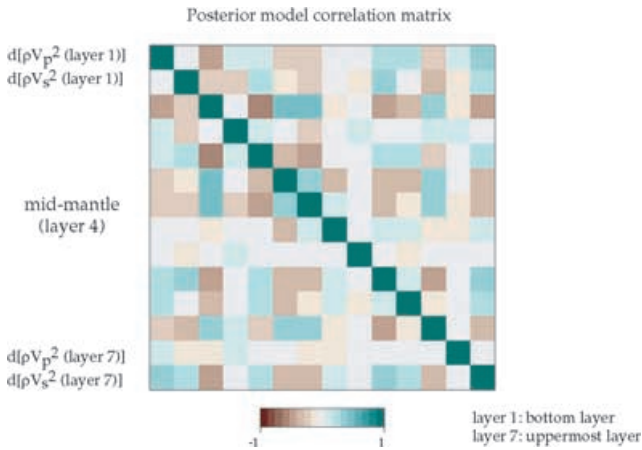

Figure 3. Correlation matrix corresponding to the real part of c_2^1 ($\delta c_2^1/c$).

results, we would need to add independent data sensitive to one or other of a given pair of correlated model parameters. The correlation matrix is an excellent tool to see what is actually resolvable and what additional data is most desirable.

The covariance matrix can also be used to obtain the variances of the model parameters (obtained from its diagonals). However, the use of a covariance matrix only makes sense when the PPD is a Gaussian distribution. A more general way of looking at variances and trade-offs is given by marginal distributions. A 1-D marginal is the probability of each value of a particular model parameter, given all possible variations of the others. The width of those posterior marginals gives a further indication on the constraint we have on each variable, and can be assimilated in error bars. A 2-D marginal shows the likelihood of each combination of values for a pair of model parameters. Computing the joint marginal of two model parameters implies an integration over all the other parameters. Fig. 4 shows 2-D marginals of some pairs of variables for the real part of c_2^1. These marginals are a robust way of looking at model parameter trade-offs. The elongated shape observed for some pairs of variables shows the trade-off between them. For instance, the top left-hand marginal of Fig. 4 shows a trade-off between δA in the lowermost layer (layer 1) and the layer above (layer 2, between 2018 and 2609 km depth) and the bottom middle marginal shows a trade-off between P anomalies (δA) in layer 4 (between 1000 and 1526 km

depth) and S anomalies (δL) in layer 3 (at depths between 1526 and 2018 km). Even with the additional constraints provided by surface waves, the upper and the lower mantle are not completely independent. The bottom left-hand marginal shows a trade-off between δL in the upper mantle (layer 7) and δA between 2018 and 2609 km depth (layer 2). We also show two pairs of model parameters that almost do not correlate in Fig. 3: δA and δL between 2018 and 2609 km depth (bottom right) and δA and δL at depths between 670 and 1000 km (top right). Neither show the elongated diagonal pattern characterizing a trade-off.

In Fig. 5, we show the 1-D marginals for a few model parameters. δA at depths between 2018 and 2609 km can take a large range of values compatible with the data. The width of the 1-D marginal is large. In this particular case, the sign of the perturbation is barely constrained. In contrast, in the upper layers, between 220 and 1000 km of depth, both P and S anomalies are better determined. If we compare the 1-D marginal and Fig. 2 for δA between 1000 and 1526 km of depth, we observe a difference. From Fig. 2, one could expect a wide range of possible values for that parameter and thus a 1-D marginal with a shape similar to that obtained for δA between 2018 and 2609 km depth. Its width is relatively large but it clearly peaks towards the edge, at a positive value. This difference between the sampling and the Bayesian interpretation of this sampling comes from the resampling of the ensemble that has to be made in order to
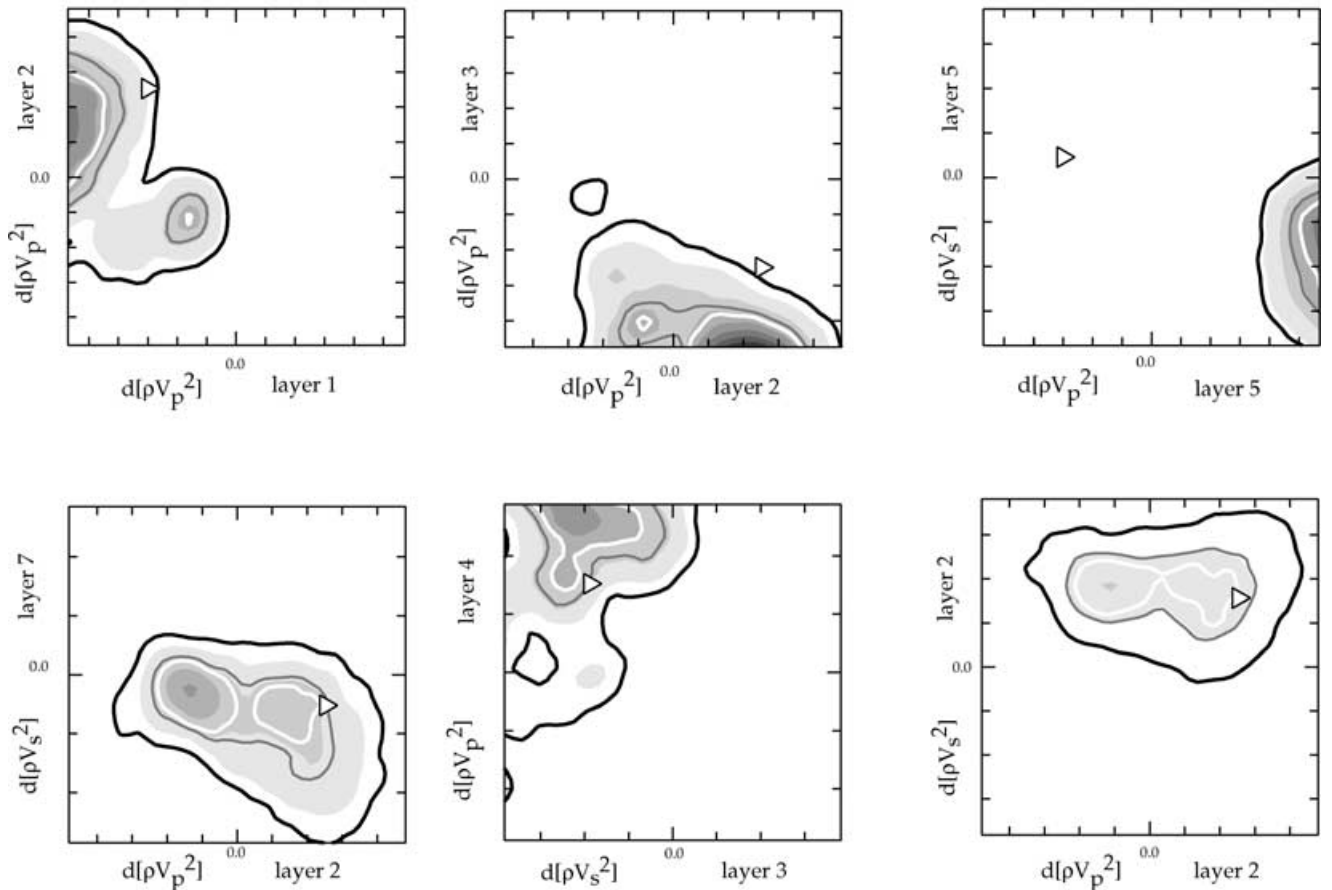

Figure 4. 2-D marginals corresponding to the real part of c_2^1 ($\delta c_2^1/c$). The white triangle denotes the values for model SB10L18. Going from inside towards the edges, the solid lines represent the 30 per cent (white), 50 per cent (grey) and 90 per cent (black) confidence levels. Parameters on the horizontal axis correspond to perturbations in elastic coefficient A (= $\delta(\rho V_p^2)$) and parameters on the vertical axis correspond to perturbations in L (= $\delta\mu = \delta(\rho V_s^2)$), with respect to PREM. The full range of the models space is shown.

1-D Marginals

lower mantle
2018 km < d < 2609 km

mid-mantle
1001 km < d < 1526 km

———— model SB10L18
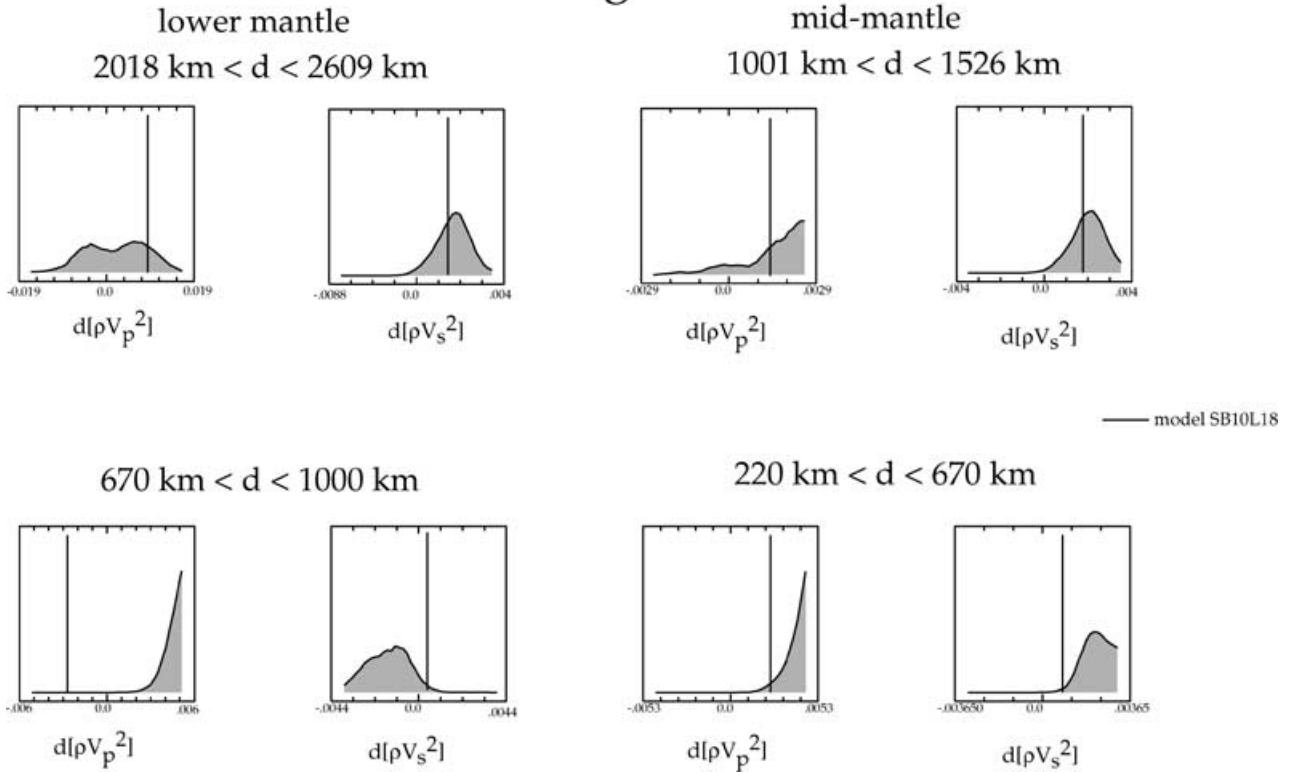
670 km < d < 1000 km

220 km < d < 670 km

Figure 5. 1-D marginals corresponding to the real part of c_2^1 ($\delta c_2^1/c$). The vertical black line is the position of model SB10L18. The full range of the models space is shown.

evaluate an approximate PPD. These marginals also show that all the parameters in the model space are not exactly Gaussian distributed. When a most likely parameter is located towards the edge of the model range, boundary effects destroy the Gaussian shape. Another strong influence on the Gaussian distribution comes from the null-space. If the model parameters are Gaussian distributed, the PPD is Gaussian. In the presence of a null-space the PPD will show an elongated valley and appear non-Gaussian distributed. Away from the edges of our sampling range, the 1-D marginals are thus a measure of the size of the null-space. The 2-D marginals and the off-diagonal elements of the correlation matrix compare quantitatively well, but the amplitudes of the correlations are affected by large non-Gaussian distributions. Using a Gaussian assumption for the PPD will underestimate the posterior uncertainties on the model parameters in the presence of a large null-space.

We did not test different parametrizations. Choosing another parametrization would probably modify the results since, as shown by the correlation matrix, all model parameters are to some extent correlated to one another. The layers we have chosen are based on those of Resovsky & Ritzwoller (1998) which approximate the optimal depth layers that can be resolved for the given depth kernels. Modifying the layers will thus only degrade the posterior covariance. The important point is that the results should only be considered with the correlation matrix.

3.2 Shear and compressional wave velocity models and error bars

In this section, we discuss mainly the most likely models. These are the models corresponding to the maximum of the 1-D marginals

and not the mean model as calculated directly by using the NA. The reason for this is that the mean model is only meaningful when the PPD is Gaussian and this is not exactly the case for all the parameters in the model space, as discussed in Section 3.1. For the same reason, we preferred to estimate the width of the 1-D marginals instead of reading them directly in the covariance matrix. We took this width as the largest distance where the amplitude of the most likely models has decreased by a factor of 1/e. It usually gives slightly larger variances than those read in the covariance matrix.

In Fig. 6, we compare the root mean square (rms) amplitude of our most likely velocity models, their robust part (the most likely model from which we subtract the uncertainties) and the rms of model SB10L18, as a function of depth. SB10L18 is a joint *P* and *S* model derived from the inversion of body waves, surface waves and normal-mode splitting data. The rms of the robust part of our models correspond to a lower limit for *S*- and *P*-model amplitudes. The size of the anomalies in SB10L18 and in our most likely model is similar. They differ the most between 220 and 670 km depth and below 1000 km for V_s. For V_p, the amplitudes are close in the top 670 km and between 1000 and 1526 km of depth. The differences are partly a result of the presence of body wave data in SB10L18.

In Fig. 7(a) we show the geographical correlation of our $d \ln V_s$ model with other *S* models (degree two): MM2-L12D8 (Resovsky & Ritzwoller 1999a), SKS12-WM13 (Su *et al.* 1994), S20RTS (Ritsema & Van Heijst 2000), SAW12D (Li & Romanovwicz 1996) and S16B30 (Masters *et al.* 1996). These models were derived from linearized inversions. For most models, in some layers, the correlation is above the 90 per cent confidence level for degree-two maps (corresponding to a correlation coefficient of 0.73, Eckhardt 1984) and there are two layers, in the mid-mantle, where the correlation
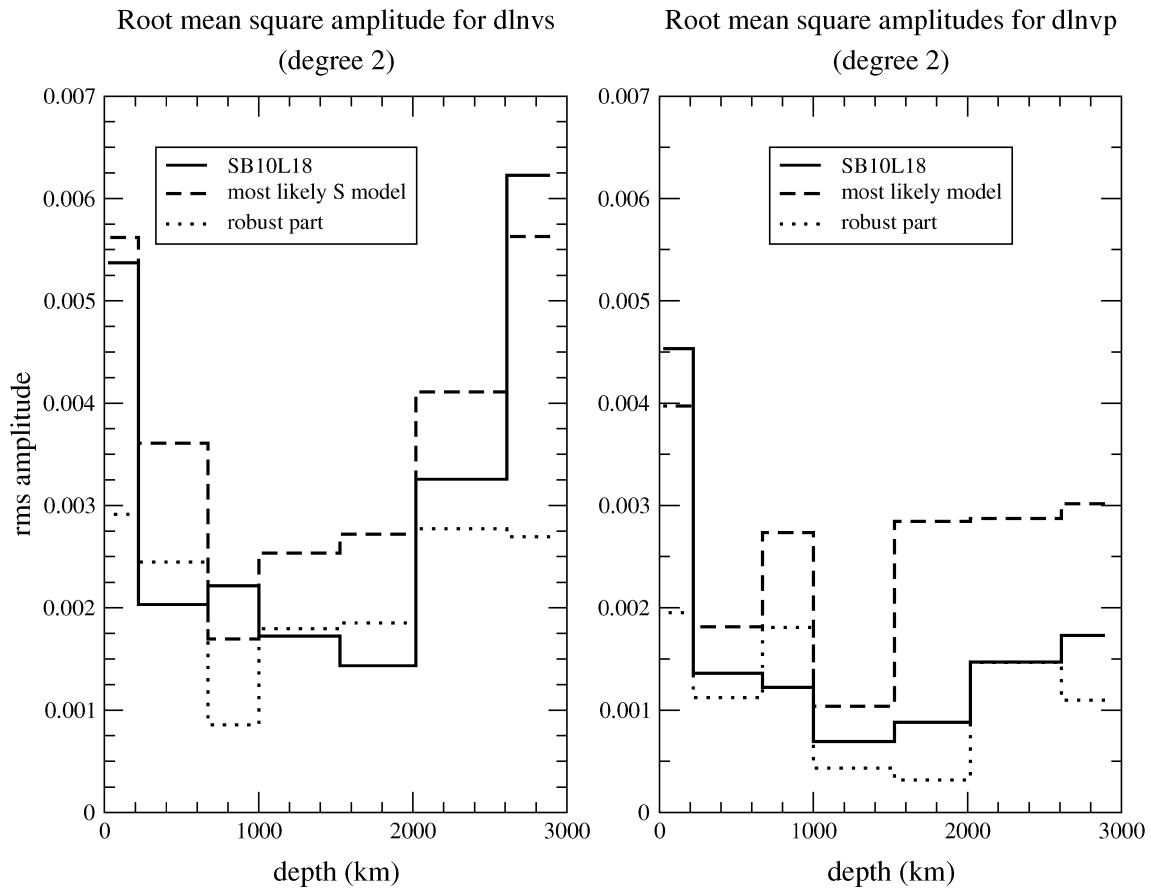
Root mean square amplitude for dlnvs
(degree 2)

Root mean square amplitudes for dlnvp
(degree 2)

Figure 6. Root mean square amplitudes of our most likely models, their robust part and model SB10L18 as a function of depth. Left, corresponds to *S* anomalies. Right, corresponds to *P* anomalies.

is very low, with any other model. One could expect it to be better for models MM2-L12D8 and S20RTS that incorporated the same set of normal-mode data as we used. This poor correlation is related to the trade-off between V_p and V_s in the mid-mantle (Fig. 3). We searched for a joint *P* and *S* model, whereas MM2-L12D8 and S20RTS assume a scaling between $d \ln V_p$ and $d \ln V_s$. These very different constraints on V_p lead to different V_p models and, in the mid-mantle, the trade-offs imply that V_s can also be very different. Fig. 7(b) shows the geographical correlation for degree two of our most likely models with model SB10L18, for both *P* and *S* since SB10L18 is a joint *P* and *S* model. It is interesting to see that the correlation coefficient between our *S* model and the *S* model of SB10L18 is above the 90 per cent confidence level in most layers. For the *P* models, the correlation is not as good, especially in the lowermost mantle where the correlation coefficient is close to zero. They correlate reasonably well between depths of 220 and 670 km and between 1000 and 1526 km.

In Fig. 8(a) and (b), we plot the maps corresponding to our most likely degree-two *S* and *P* models in the seven layers we use. A robust feature from all tomographic models to date is that the degree-two structure dominates the two lowermost layers ($2609 \leq d \leq 2891$ km and $2018 \leq d \leq 2609$ km) and in the transition zone (Resovsky & Ritzwoller 1999a). These maps are thus good approximations to complete tomographic models only at those depths. As we see from the correlation coefficient in Fig. 7(b), both *S* models agree quite well at most depths. In contrast, the two *P* models differ much more.

In Fig. 9(a) we plot the correlation between our most likely *P* and *S* models. The correlation is significantly high (above the 90 per cent

confidence level) only between depths of 220 and 670 km. The lowest correlations are situated in the lowermost and uppermost layers. This is not representative in the uppermost mantle because degree-two structure is not dominant there. In contrast, the lowermost mantle is believed to be dominated by that degree. We cannot, however, conclude directly that there is no correspondence between *P* and *S* anomalies in the lowermost mantle. One of the advantages of using the NA is that it provides error bars on the models. Within these error bars, there may be models compatible with the data that have a higher $V_s - V_p$ correlation. A better way to look at that correlation is thus by taking into account the uncertainties in the models. To take into account all the models, we sample δA and δL within their estimated error bars with a random number generator, we deduce the corresponding $d \ln V_s$ and $d \ln V_p$, and we compute the correlation coefficient for all possible combinations. That distribution of correlation values can be plotted as a histogram. It is interesting to note that the histograms are largely independent of how we sampled the models (uniformly, Gaussian or corresponding to the actual 1-D marginals). We take the median of the correlation coefficient and we estimate its uncertainty. The uncertainty of the median is obtained by computing its scaled median absolute deviation (SMAD) (Bevington 1969). We use the SMAD as the uncertainty on the overall correlation coefficient. In Table 1 we list the median correlation coefficients and their uncertainty at different depths and Fig. 9(b) gives the histograms for different depths. In our lowermost layer, where our most likely *P* and *S* models do not correlate (the correlation coefficient was -0.417), we see that the median value is also very low (-0.535) and lots of models are anticorrelated. The

(a) Correlation between our most likely
S model and other S models (degree 2)

(b) Correlation with model SB10L18
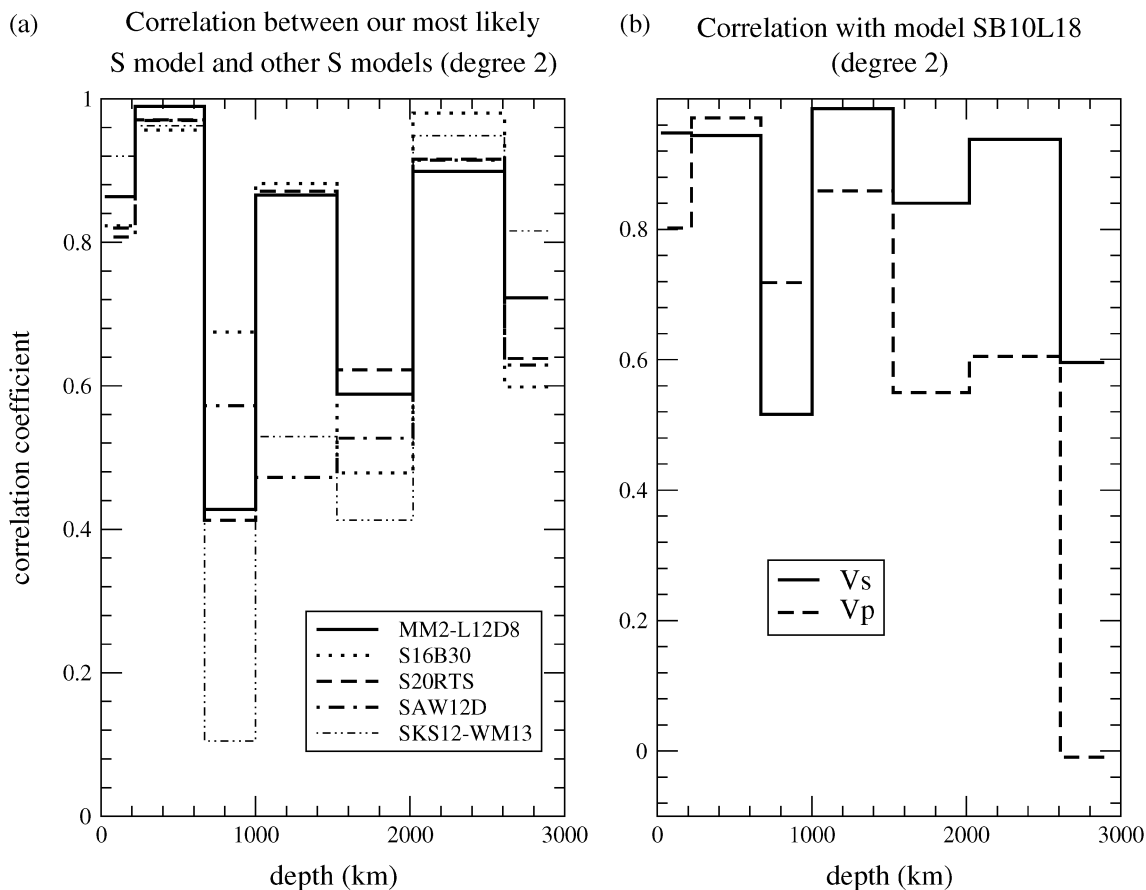(degree 2)

Figure 7. Correlation coefficient between our most likely models and other models as a function of depth. Left, represents the correlation between our most likely *S* model with five other *S* models. Right, represents the correlation between our most likely models with the joint *P* and *S* model SB10L18.

uncertainty is, however, very large and there are a few models compatible with the data that correlate well. There are models in the layers above that correlate well and some correlate significantly. In the uppermost layer, correlation is poor again, but there degree two is far from dominant. This is one illustration of the importance of error bars in tomographic models.

Error bars for the spherical harmonic components of $d \ln V_s$ and $d \ln V_p$ can be derived easily from those on dA_s^t and dL_s^t. In Fig. 10 we show the relative error bars for the rms amplitude, $d(\text{rms})/\text{rms}$, for both shear and compressional wave velocities. This represents the size of the error bars on the rms relative to the size of the most likely model. The error bars are large, especially for V_p. These uncertainties are mainly a result of the large null-space associated with our problem. It shows what can be determined by the data alone. Prior information can of course reduce the null-space, but we argue that choosing a model should be based on physical information rather than a subjective damping parameter. Unless such a physical prior information exists, it is preferable to consider all models compatible with the data. Another way to reduce the size of the null-space is of course by adding more data. We expect that including body wave data will significantly reduce the uncertainties.

Perturbations in V_s are believed to be larger than perturbations in V_p. The value of their ratio $R = d \ln V_s/d \ln V_p$ is commonly used as a diagnostic as to whether the heterogeneities in the mantle have a chemical or thermal origin. The value of R in the deep mantle is still a controversy. A low ratio could be explained by a thermal origin of the anomalies and a high value (above 2.5) could indicate a chemical component in the heterogeneities. Looking at various studies, there

is a large variety of values for R. A good review on the subject can be found in Masters *et al.* (2000). Because different authors compute R in different ways, Masters *et al.* (2000) recalculated a spherically averaged R for various models. Generally, studies using body wave traveltime data only prefer a high value of R in the lowermost mantle. Robertson & Woodhouse (1996) use ISC data and find a ratio slowly increasing from 1.7 to 2.5 for depths between 600 and 2000 km. Bolton (1996) uses long-period body wave data and his results also show an increase of R with depth up to a value slightly below 3.5 at the bottom of the mantle. Both studies were constrained inversions, i.e. a perfect proportionality between P and S anomalies at every depth was imposed but R was allowed to change. Su & Dziewonski (1997) use ISC data, long-period body wave and surface wave data to perform an unconstrained inversion for bulk sound and shear wave speed. They obtain a value of $d \ln V_s/d \ln V_p$ of almost 3.5 in the lowermost mantle. Saltzer *et al.* (2001) employ ISC data to produce P and S models of the mantle. They distinguish between regions where there has been subduction over the last 120 Myr and where there has not. They find a peak value of $R = 3$ around 2200 km of depth in non-slab regions and a ratio smaller than 2 at all depths in slab regions. There are two models using ISC data that show a low ratio at all depths. These are the models of Vasco & Johnson (1998) and Kennett *et al.* (1998). Their values of R are smaller than 1.5, and even smaller than 1 for Vasco & Johnson (1998). When normal modes are included in the data set, the tendency observed in joint inversions is to have a more modest ratio in the lowermost mantle (model SB10L18), except for Romanowicz (2001) who finds a value between 1 and 2 everywhere, but at depths greater than 2000 km
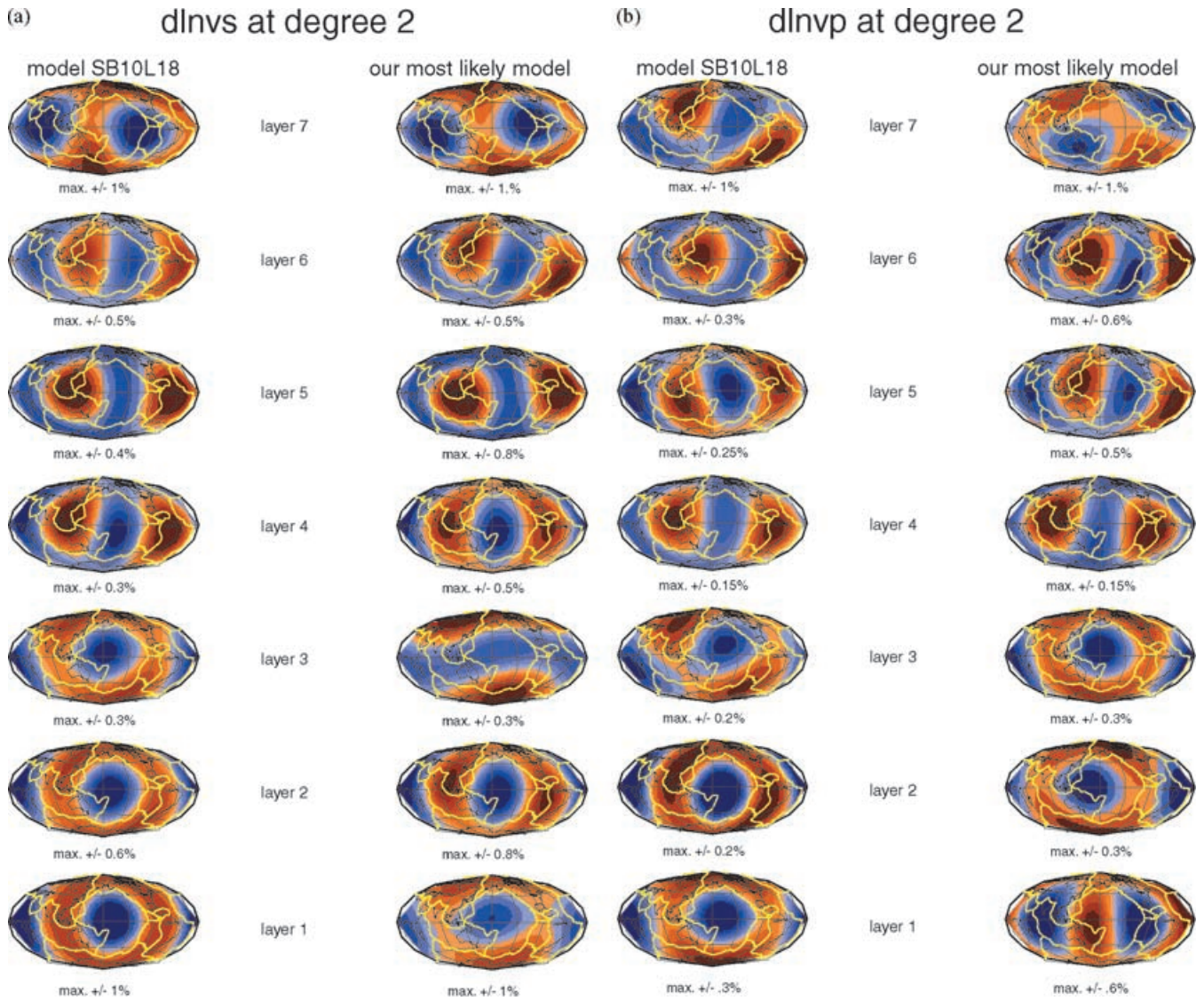
Figure 8. Degree two maps of our most likely *P* and *S* models compared with degree-two maps of models SB10L18. Layer 1 corresponds to the lowermost and layer 7 to the uppermost mantle.

R is larger than 2.5. Model SB10L18 was obtained from the joint inversion of bulk sound and shear wave speed, whereas Romanowicz (2001) performed inversions for V_p and V_s directly. In their paper, Masters *et al.* (2000) also observe that constrained inversions for bulk sound and shear wave speed usually give *P* and *S* models that correlate significantly while there is less correlation in inversions for V_p and V_s.

We compute $R = d\ln V_s/d\ln V_p$ on a 10 deg × 10 deg grid. We take into account all the models obtained for V_s and V_p, in the same way we did to compute the correlation between all of our *P* and *S* models. We take a series of values of δA and δL within their estimated error bars, on each gridpoint, we compute the corresponding $d\ln V_s$ and $d\ln V_p$ models and *R* for all the possible combinations. We determine the median of that distribution of values, which we take as the spherically averaged estimate of *R*. The SMAD is used to derive the uncertainty on *R* (as in Masters *et al.* 2000). We find that *R* takes modest values in the lowermost mantle (see Fig. 11, dotted line). The question is whether *R* is low in the lowermost mantle (where degree-two structure is dominant) because the correlation is low or because the normal-mode data generally prefer a lower ratio.

To answer that, we compute *R* by only taking the models that correlate significantly (above 0.73) in one particular layer. The values are plotted in Fig. 11 (solid line). We observe an increase of *R* with depth in the top 1500 km of the mantle, taking values between 1 and 1.75, and modest values in the lowermost mantle. This shows that normal-mode data favour low values for *R* in the deeper mantle, in contradiction with Romanowicz (2001), who finds $d\ln V_s/d\ln V_p$ up to 3.5 at depths >2000 km, using degree-two normal-mode splitting data and a layered parametrization. The possible reasons for this difference are that Romanowicz does not include surface wave measurements in her data and introduces strong prior information in the inversions (the damping was chosen so that $d\ln V_s/d\ln V_p$ matches the range 1.5–2 in the top 1500 km, which is somewhat higher than what we find).

4 CONCLUSION

The aim of this paper is to explore a model space with a direct search method in order to identify good data-fitting isotropic Earth models. We used the neighbourhood algorithm developed by Sambridge
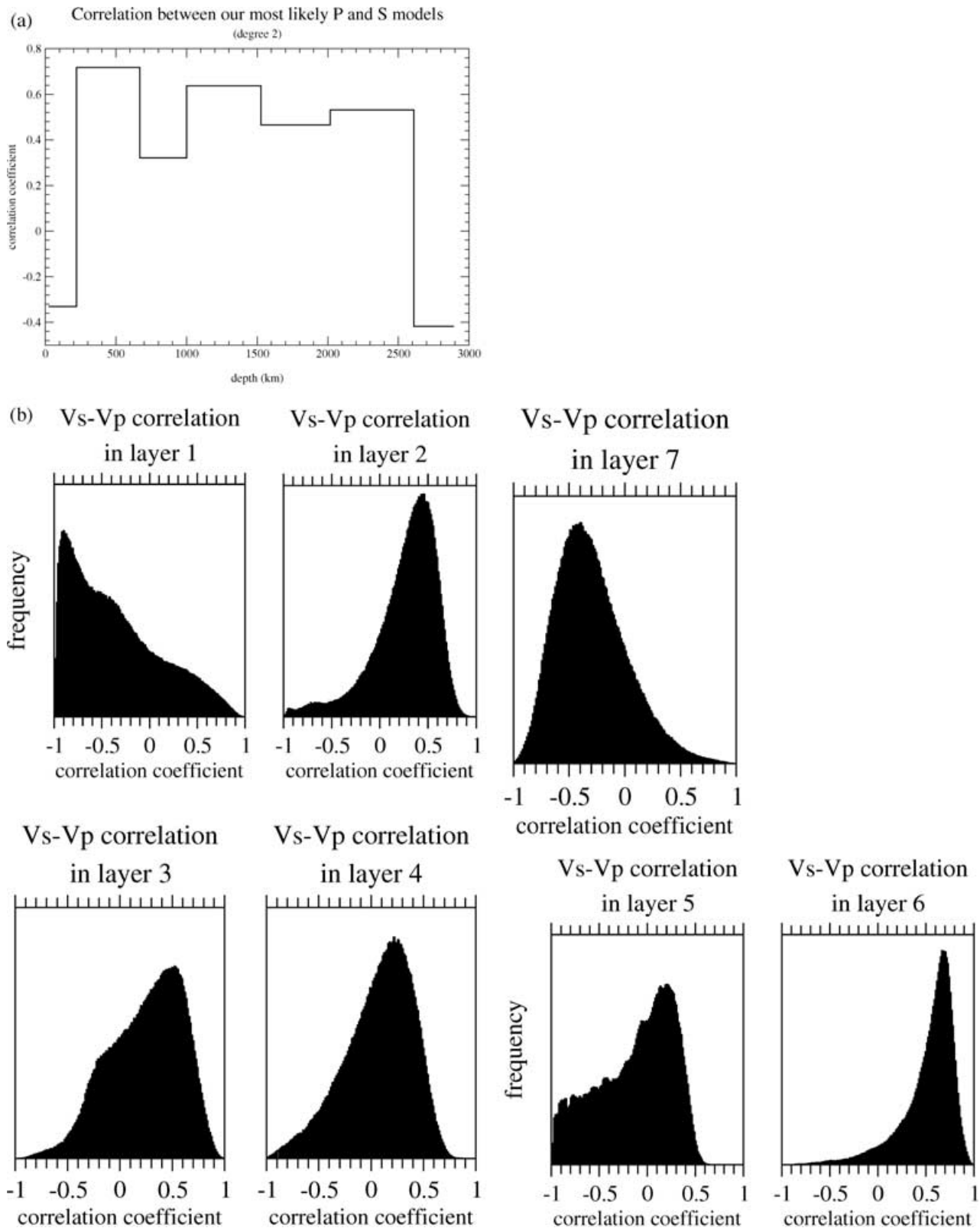
Figure 9. Left: correlation coefficient between our most likely *P* and *S* models as a function of depth; right: distribution of $V_s - V_p$ correlation coefficient between all the models compatible with the data as a function of depth.

(1999a,b), which is a new derivative-free direct search technique that preferentially samples the good data-fitting regions of a model space. A Bayesian approach is used subsequently in order to extract robust information from the ensemble of models generated. We ex-

amine the posterior marginal probability density functions, the variances of the various model parameters and the correlations among them. The whole model space, including the null-space, is sampled within reasonable bounds and the error bars are consequently more

Table 1. Correlation coefficient between all models generated within their error bars. The second column gives the median of the distribution and the third column gives its robustness.

Depth (km)	Median (all models)	SMAD
$2609 < d < 2891$	-0.535	0.425
$2018 < d < 2609$	0.36	0.30
$1526 < d < 2018$	0.205	0.36
$1001 < d < 1526$	0.20	0.27
$670 < d < 1001$	0.003	0.42
$220 < d < 670$	0.62	0.18
$24 < d < 220$	-0.29	0.36

realistic than traditional inversion error estimates. This new technique appears to be very efficient in finding the best data-fitting regions in a high dimensional space (provided the size of the model space has been established). It is easy to tune since there are only two tuning parameters but they have to be chosen carefully to avoid the search being trapped in a local minimum and to importance sample the entire parameter space, while not reducing the efficiency of the algorithm. The optimal values have to be found by trial and error. The subsequent use of the Bayesian algorithm does not require any further solutions of the forward problem. The parameter space is resampled instead, using only information from the initial survey of the model space. The accuracy of the Bayesian integrals will depend on the way in which the model space was initially sampled.

We applied the neighbourhood algorithm to the search of isotropic mantle shear and compressional wave velocity models, using recent normal-mode splitting measurements and fundamental-mode phase velocity data. We found an ensemble of joint *P* and *S* models (spherical harmonic degree two only) for which posterior marginal probability density functions, correlation and covariances were computed. 1-D marginals give information on how well a parameter is constrained and shows whether it is Gaussian distributed or not. They are used to infer error bars on the various model parameters. 2-D marginals show the trade-offs among pairs of model parameters. The posterior covariance matrix obtained under a Gaussian assumption gives a fair representation of the correlation, although error
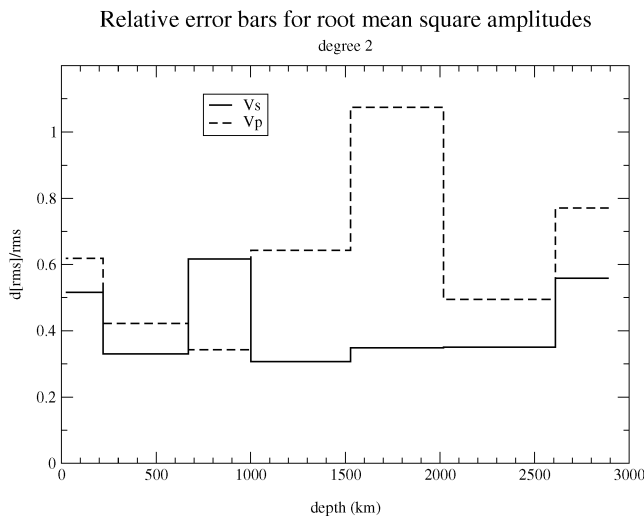

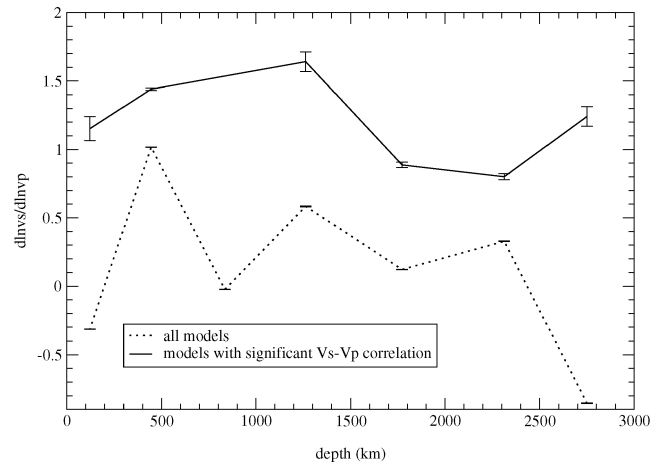Figure 11 title: dlnvs/dlnvp with error bars

Figure 11. Ratio between degree two $d \ln V_s$ and $d \ln V_p$ as a function of depth.

bars may be underestimated in the case of a strongly non-Gaussian distribution. The uncertainties and correlations constitute essential information in order to make a meaningful analysis of the models obtained. We see, for instance, that there is a correlation between parameters of the lower mantle and parameters of the upper mantle. This implies that we could improve our models by adding data, sensitive exclusively to either the upper or lower mantle in order to decorrelate those parameters. Our most likely *S* model is highly correlated with other *S* models such as MM2-L12D8, SKS12-WM13, S20RTS, SAW12D or S16B30, except where there is a high trade-off between *P* and *S* perturbations. The correlation with the recent *S* model SB10L18 is very high at most depths but our most likely *P* model is very different from the *P* model of SB10L18 in most layers. Degree-two error bars on the rms velocity perturbations of our mean models are quite large, especially for *P*. The correlation between our most likely *P* and *S* model is low but among all the models generated and compatible with the data, there are some that have a high $V_p - V_s$ correlation. We calculated the ratio $R = d \ln V_s / d \ln V_p$. We find an increase with depth in the top 1500 km up to a value of 1.75. Deeper in the mantle, there is a decrease and R oscillates between 0.8 and 1.3. Most models using body wave data alone seem to find a high value for R in the deep mantle. Our study, for which only surface wave and normal-mode data have been employed, tends to favour much lower values. The model of Masters *et al.* (2000) obtained from surface waves, normal-mode and body wave data thus gives an intermediate ratio at these depths.

We have a powerful new tool to explore a model space, including the null-space, and to estimate ranges of 'good' data-fitting models. In the absence of true physical information, we prefer to consider the full range of models consistent with the data. Correlations between model parameters can be computed and give valuable indications of what kind of independent data should be added to constrain the models better. Because our problem can be solved spherical harmonic coefficient by spherical harmonic coefficient, it is trivial to parallelize the procedure resulting in huge time savings for computing a full tomographic model.

Figure 10 title: Relative error bars for root mean square amplitudes — degree 2

Figure 10. Relative uncertainties for the root mean square amplitude of our most likely *S* model (solid line) and our most likely *P* model (dashed line) as a function of depth.

Reviews and comments by K. Yoshizawa, J.A. Snoke and M. Sambridge were very helpful and are gratefully acknowledged.

REFERENCES

Anderson, O.L., Schreiber, E., Liebermann, R.C. & Soga, M., 1968. Some elastic constant data on minerals relevant to geophysics, *Rev. Geophys.,* **6,** 491–524.

Backus, G. & Gilbert, F., 1968. The resolving power of gross Earth data, *Geophys. J. R. astr. Soc.,* **16,** 169–205.

Bevington, P.R., 1969. *Data Reduction and Error Analysis for the Physical Sciences,* McGraw-Hill, New York.

Bolton, H., 1996. Long period travel times and the structure of the mantle, *PhD thesis,* La Jolla, CA.

Dahlen, F.A. & Tromp, J., 1999. *Theoretical Global Seismology*, Princeton Univ. Press, Princeton, NJ.

Deal, M., Nolet, G. & van der Hilst, R.D., 1999. Slab temperature and thickness from seismic tomography 1. Method and application to Tonga, *J. geophys. Res.,* **104,** 28 789–28 802.

Dziewonski, A.M. & Anderson, D.L., 1981. Preliminary reference Earth model, *Phys. Earth planet. Inter.,* **25,** 25 297–25 356.

Eckhardt, D.H., 1984. Correlations between global features of terrestrial fields, *Math. Geol.,* **16,** 155–171.

Edmonds, A.R., 1960. *Angular Momentum and Quantum Mechanics,* Princeton Univ. Press, NJ.

Ekström, G., Tromp, J. & Larson, E.W.F., 1997. Measurements and global models of surface wave propagation, *J. geophys. Res.,* **102,** 8137–8157.

Kennett, B.L.N., Widiyantoro, S. & van der Hilst, R., 1998. Joint seismic tomography for bulk sound and shear wave speed in the Earth's mantle, *J. geophys. Res.,* **103,** 12 469–12 493.

Laske, G. & Masters, G., 1996. Constraints on global phase velocity maps from long-period polarization data, *J. geophys. Res.,* **101,** 16 059–16 075.

Li, X.D. & Romanovwicz, B., 1996. Global mantle shear-velocity model developed using nonlinear asymptotic coupling theory, *J. geophys. Res.,* **101,** 22 245–22 272.

Love, A.E.H., 1927. *A Treatise on the Theory of Elasticity,* 4th edn, p. 643, Cambridge Univ. Press, Cambridge.

Masters, G., Johnson, S., Laske, G. & Bolton, H.A., 1996. A shear-velocity model of the mantle, *Phil. Trans. R. Soc. Lond.,* A., **354,** 1385–1411.

Masters, G., Laske, G., Bolton, H. & Dziewonski, A., 2000. The relative behaviour of shear velocity, bulk sound speed, and compressional velocity in the mantle: Implications for chemical and thermal Structure, in *Earth's Deep Interior: Mineral Physics and Tomography from the Atomic to the Global Scale, Seismology and Mineral Physics, Geophys. Monogr. Ser.,* Vol. 117, pp. 63–87, ed. Karato, S., AGU, Washington, DC.

Mochizuki, E., 1986. The free oscillations of an anisotropic and heterogeneous Earth, *Geophys. J. R. astr. Soc.,* **86,** 167–176.

Mooney, W.D., Laske, G. & Masters, G., 1998. CRUST 5.1: a global crustal model at 5 degrees by 5 degrees, *J. geophys. Res.,* **103,** 727–748.

Resovsky, J.S. & Ritzwoller, M.H., 1998. New and refined constraints on three-dimensional Earth structure from normal modes below 3 mHz, *J. geophys. Res.,* **103,** 783–810.

Resovsky, J.S. & Ritzwoller, M.H., 1999a. A degree 8 mantle shear velocity model from normal mode observations below 3 mHz, *J. geophys. Res.,* **104,** 100–110.

Resovsky, J.S. & Ritzwoller, M.H., 1999b. Regularization uncertainty in density models estimated from normal mode data, *Geophys. Res. Lett.,* **26,** 2319–2322.

Resovsky, J.S. & Trampert, J., 2002. Reliable mantle density error bars: an application of the neighbourhood algorithm to normal mode data, *Geophys. J. Int.,* in press.

Ritsema, J. & Van Heijst, H.J., 2000. Seismic imaging of structural heterogeneity in the Earth's mantle: evidence for large-scale mantle flow, *Sci. Progr.,* **83,** 243–259.

Robertson, G.S. & Woodhouse, J.H., 1996. Ratio of relative *S* to *P* velocity heterogeneity in the lower mantle, *J. geophys. Res.,* **101,** 20 041–20 052.

Romanowicz, B., 2001. Can we resolve 3D heterogeneity in the lower mantle?, *Geophys. Res. Lett.,* **28,** 1107–1110.

Saltzer, R.L., van der Hilst, R. & Kárason, H., 2001. Comparing *P* and *S* wave heterogeneity in the mantle, *Geophys. Res. Lett.,* **28,** 1335–1338.

Sambridge, M., 1998. Exploring multidimensional landscapes without a map, *Inverse Problems,* **14,** 427–440.

Sambridge, M., 1999a. Geophysical inversion with a neighbourhood algorithm—I. Searching a parameter space, *Geophys. J. Int.,* **138,** 479–494.

Sambridge, M., 1999b. Geophysical inversion with a neighbourhood algorithm—II. Appraising the ensemble, *Geophys. J. Int.,* **138,** 727–746.

Su, W.-J. & Dziewonski, A.M., 1997. Simultaneous inversion for 3D variations in shear and bulk velocity in the mantle, *Phys. Earth planet. Inter.,* **100,** 135–156.

Su, W.-J., Woodward, R.L. & Dziewonski, A.M., 1994. Degree 12 model of shear velocity heterogeneity in the mantle, *J. geophys. Res.,* **99,** 6945–6980.

Tanimoto, T., 1986. Free oscillations of a slightly anisotropic Earth, *Geophys. J. R. astr. Soc.,* **87,** 493–517.

Tarantola, A., 1987. *Inverse Problem Theory, Methods for Data Fitting and Model Parameter Estimation,* Elsevier, Amsterdam.

Trampert, J., 1998. Global seismic tomography: the inverse problem and beyond, *Inverse Problems,* **14,** 371–385.

Trampert, J. & Woodhouse, J.H., 1995. Assessment of global phase velocity maps of Love and Rayleigh waves between 40 and 150 s, *Geophys. J. Int.,* **122,** 675–690.

Trampert, J. & Woodhouse, J.H., 1996. High resolution global phase velocity distributions, *Geophys. Res. Lett.,* **23,** 21–24.

Trampert, J. & Woodhouse, J.H., 2001. Assessment of global phase velocity models, *Geophys. J. Int.,* **144,** 165–174.

van Heijst, H.J. & Woodhouse, J.H., 1999. Global high-resolution phase velocity deistributions of overtone and fundamental-mode surface waves determined by mode branch stripping, *Geophys. J. Int.,* **137,** 601–620.

Vasco, D.W. & Johnson, L.R., 1998. Whole Earth structure estimated from seismic arrival times, *J. geophys. Res.,* **103,** 2633–2671.

Wong, Y.K., 1989. Upper mantle heterogeneity from phase and amplitude data of mantle waves, *PhD thesis,* Harvard Univ., Cambridge, MA.

Woodhouse, J.H. & Dahlen, F.A., 1978. The effect of a general aspherical perturbation on the free oscillations of the Earth, *Geophys. J. R. astr. Soc.,* **53,** 335–354.